Bathymetric Mapping in Coastal Waters with Satellite Images: A Case Study in the Mexican Caribbean

Jean-François Mas[1], Azucena Pérez Vega[2]

[1] Centro de Investigaciones en Geografía Ambiental, Universidad Nacional Autónoma de México, Morelia, Mexico - jfmas@ciga.unam.mx
[2] Departamento de Geomática e Hidráulica, Universidad de Guanajuato, Guanajuato, Mexico - azupv@ugto.mx

Keywords: Bathymetry, Remote Sensing, Multispectral Images, Ratio Transformation, Empirical Algorithm, Mexican Caribbean.

Abstract

In this study, bathymetric models were developed in coastal waters of the Mexican Caribbean, using an empirical algorithm and satellite images from Landsat 9, Sentinel-2 and SuperDove CubeSats. The model used is based on the relationship between the blue and green spectral bands and was adjusted with depth data taken *in situ* in the coastal area of Mahahual, Quintana Roo using linear regression, regularized regression and random forest approaches. The study showed that the model enables the estimation of depth relatively accurately, up to 20 meters. Sentinel-2 and random forest presented the best performance, with an RMSE error of 0.79 meters, followed by Landsat (0.88 m) and SuperDove (1.02 m). The most significant errors occurred at shallow depths of less than 5 m or greater than 20 m. Preprocessing of the images, particularly sunlight correction and spatial filtering, was crucial to improving the results. Remote sensing offers a very economical alternative for mapping bathymetry in shallow, low-turbid coastal areas.

1. Introduction

Knowledge of bathymetry is crucial in oceanographic research, as it provides detailed information about seafloor topography, which is essential for understanding the dynamics of underwater processes. Additionally, bathymetric knowledge is crucial for safe navigation, planning marine infrastructure, and sustainable management of aquatic resources. Conventionally, hydrographic survey methods using acoustic systems aboard ships are employed for bathymetric surveys, but these require high-cost resources. Space technology has provided a cost-effective alternative for mapping near-coastal bathymetry (Ashphaq et al., 2021).

Remote sensing is one of the most promising tools for mapping bathymetry in shallow coastal waters due to its broad coverage, low cost, and repeatability (Casal et al., 2020; Jagalingam et al., 2015). In recent years, satellite launches such as Landsat 9, Sentinel-2, and SuperDove CubeSats have provided high spatial and spectral resolution imagery, available free of charge.

Analytical algorithms for bathymetric mapping using remote sensing data can be found in the literature, such as those by Lyzenga (1978; 1981), Lyzenga et al. (2006), and Philpot (1989). However, these analytical methods require input parameters such as water column properties, atmospheric conditions, and seabed material, making them difficult to apply. Several empirical algorithms have also been developed (Su et al., 2008; Stumpf et al., 2003). Compared to analytical methods, empirical approaches, such as the method described by Stumpf et al. (2003) later, require fewer parameters and are more straightforward to implement. In this study, we use a ratio transform algorithm capable of estimating depths up to 25 m in clear water according to Jagalingam et al.2015.

The objective of this study is to evaluate the performance of an empirical algorithm for estimating depth in a coastal area of the Mexican Caribbean using Landsat 9, Sentinel-2, and SuperDove CubeSat imagery.

2. Materials

Bathymetric data from Merediz-Alonso (2012), available on CONABIO's geoportal (http://geoportal.conabio.gob.mx/descargas/ mapas/imagen/96/punbmahdm11gw), were used. These data report sea depth in the coastal zone of Mahahual, Quintana Roo, in the Mexican Caribbean (see Figure 1).

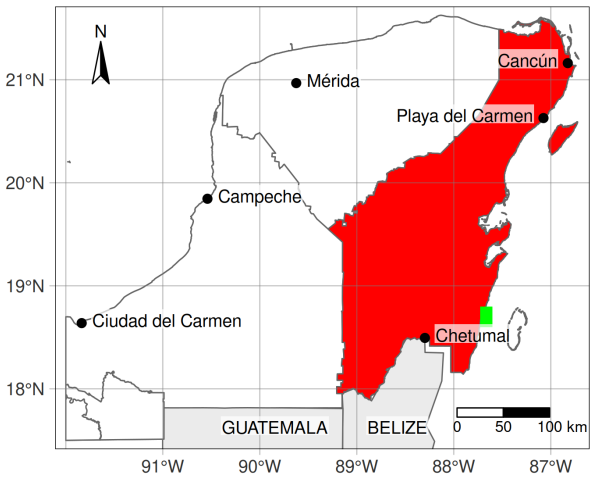

Figure 1. Study area. The state of Quintana Roo in the Yucatán Peninsula, southeastern Mexico, is highlighted in red. The study area is located 70 km from Chetumal.

To collect these data, the authors used a Lowrance LCX-17M echosounder connected to an external LGC-2000 GPS antenna. They conducted perpendicular transects along the coast, recording depth and location. The data were later processed using Sonar Viewer software and converted into a digital point map in vector format.

Tidal prediction tables from the Mexican Navy (available at https://oceanografia.semar.gob.mx/estaciones.html) were consulted. Landsat 9, Sentinel-2, and SuperDove CubeSat images Equipo Planeta (2017), processed to surface reflectance level after atmospheric correction, were used. The main characteristics of these images are summarised in Table 1.

Band	Landsat 8/9	Sentinel-2	SuperDove (PSB.SD)
Coastal blue	430-450 (30m)	434–454 (60m)	431–452 (3m)
Blue	450-510 (30m)	439–533 (10m)	465–515 (3m)
Green	530-590 (30m)	538–583 (10m)	513-549 (3m)
Green			547-583 (3m)
Yellow			600–620 (3m)
Red	640-670 (30m)	650–680 (10m)	650–680 (3m)
Red edge		698–713 (20m)	697–713 (3m)
Red edge 2		733–748 (20m)	
Red edge 3		773–793 (20m)	
Near Infrared		785–900 (10m)	
Near Infrared	850-880 (30m)	848–882 (20m)	845–885 (3m)
Water vapour		930–950 (60m)	
SWIR Cirrus	1360-1380 (30m)	1365–1395 (60m)	
SWIR	1570-1650 (30m)	1565–1655 (60m)	
SWIR	2110-2290 (30m)	2100–2280 (60m)	
Panchromatic	500-680 (15m)		
Thermal Infrared	10600-11190 (100m)		
Thermal Infrared	11500-12510 (100m)		
Acquisition time	10:00 to 10:30	10:30 to 11:00	9:30 to 10:30

Table 1. Characteristics of the images used in the study (spectral and spatial resolution, time of passage).

Image processing, spatial and statistical analyses, and graph generation were performed using R version 4.4.1 (R Core Team, 2025).

3. Methods

We selected images with minimal or no cloud cover, no apparent wave features, and clear water from their respective portals: EarthExplorer for Landsat (https://earthexplorer.usgs.gov), Planet Explorer for SuperDove (https://www.planet.com), and Copernicus Open Access Hub for Sentinel-2 (https://scihub.copernicus.eu/dhus).

The general procedure for deriving bathymetry included masking land and cloud areas, correcting wave glint effects, spatial filtering, and fitting a linear model to estimate depth. Subsequently, we mapped bathymetry and assessed the algorithm's performance by calculating depth estimation error (Figure 2). The methods used in each step are described in detail in the following sections.

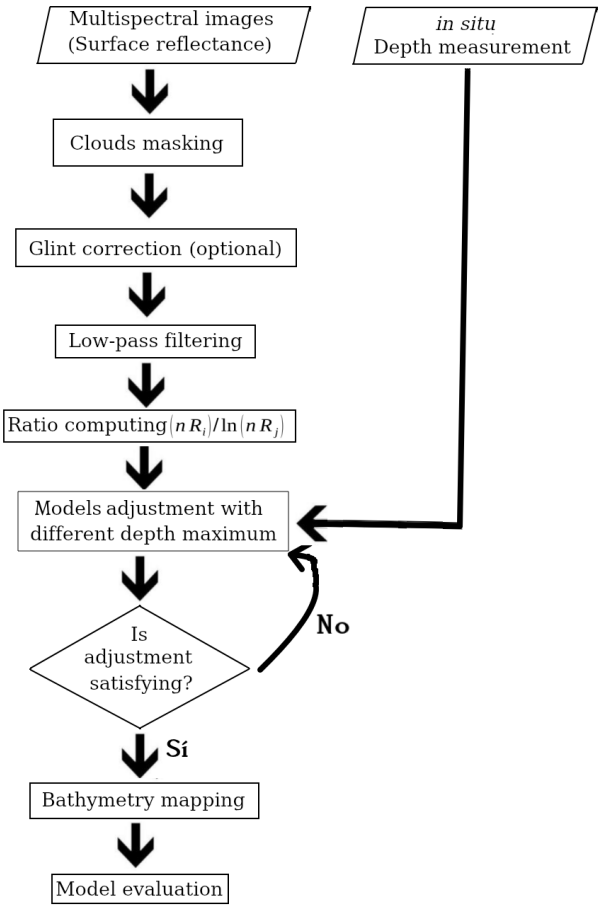

Figure 2. Flowchart describing the main processing steps for bathymetry derivation.

3.1 Image Masking and Preprocessing

Land and cloud masks were applied using image quality layers. For Landsat, the QA band was used to create water and cloud masks (including dilated clouds, cirrus clouds, and shadows), retaining only cloud-free water pixels. Digital numbers were converted to reflectance using gain and offset values. Similar operations were performed for Sentinel-2 (using the SCL layer) and SuperDove (using the UMD auxiliary image). Metadata-derived gain values were used to obtain surface reflectance images of cloud-free water areas.

3.2 Wave Glint Correction

An optional correction was applied to reduce sun glint effects caused by waves using Hedley et al.'s (2005) algorithm. This method corrects visible bands using a near-infrared (NIR) reference band, assuming water is opaque in the NIR range. A linear regression between the NIR and visible bands over deep water areas was used to estimate surface reflectance. A minimum NIR value (MinIRC) was specified to exclude glint-free conditions.

A low-pass spatial filter (3x3 moving average) was then applied to smooth reflectance values.

3.3 Ratio Transform Algorithm

Stumpf et al. (2003) developed a ratio transform algorithm for bathymetry estimation, capable of mapping depths beyond 25

m in clear water and efficiently assessing turbid coastal depths. The algorithm uses two spectral bands to reduce parameter dependency, leveraging differences in diffuse attenuation coefficients. The ratio between band reflectances (typically blue and green) varies with depth, minimising errors from atmospheric and water column variability. The equation used is:

$$Z = m_0 + m_1 \cdot \ln\left(\frac{n \cdot R_i}{R_j}\right), \quad (1)$$

where Z = depth
R_i, R_j = reflectances of bands i and j
Xn = constant ensuring positive logarithm
m_0, m_1 = empirical coefficients

In addition to linear regression, we employed two machine learning approaches: regularized regression and random forest. In the context of univariate regression, both methods offer distinct advantages over conventional linear regression. Regularized regression, when extended to accommodate polynomial terms, applies constraint-based regularization to mitigate overfitting in polynomial models. By incorporating L1 (Lasso) or L2 (Ridge) penalties, or a composite penalty, this approach automatically shrinks higher-order polynomial coefficients toward zero, effectively balancing model complexity against predictive performance through cross-validated hyperparameter tuning. In contrast, random forest represents a fundamentally different machine learning paradigm that constructs an ensemble of decision trees through bootstrap aggregation and feature randomization. This non-parametric method inherently captures complex nonlinear patterns and interaction effects without requiring explicit specification of functional forms, making it particularly valuable when the underlying relationship between variables deviates from simple polynomial approximations. Both techniques provide robust alternatives to standard linear regression, with regularized polynomial regression offering controlled flexibility within the familiar linear model framework. At the same time, random forest delivers greater adaptability to complex data structures through its ensemble-based architecture.

Outliers (top/bottom 1% of ratio values) were removed to exclude non-water pixels. Coefficients m_0 and m_1 were determined via linear regression with *in situ* bathymetry. Iterative models were fitted, adjusting maximum depth thresholds to identify linearity limits. Models with/without glint correction and filtering were compared.

Tidal corrections were omitted due to uncertainty in original data processing. Tide tables for Mahahual (MAHA1703) indicated minimal sea level differences (4–5 cm) during image acquisition, implying any systematic error would not affect inter-image comparisons.

4. Model Evaluation

Depth estimation accuracy was assessed using root mean square error (RMSE) and the mean absolute error (MAE):

$$RMSE = \sqrt{\frac{1}{N}\sum_{i=1}^{N}(O_i - P_i)^2}, \quad (2)$$

$$MAE = \frac{1}{N}\sum_{i=1}^{N}|O_i - P_i|, \quad (3)$$

where $RMSE$ = root mean square error
MAE = mean absolute error
O_i = observed depths at point i
P_i = predicted depths at point i

Both metrics provide complementary assessments of prediction error magnitude. RMSE emphasizes larger errors due to its squaring of residuals, while MAE offers a more robust interpretation, representing the average absolute prediction error. These metrics are widely accepted in statistical practice for quantifying model accuracy and facilitate direct comparison between different modeling approaches on the same scale as the response variable. RMSE and MAE were computed for each image type and method, and residual spatial distribution was visualized.

5. Results

The Mahahual bathymetry dataset comprised 2,844 points, with 255 shoreline points (zero depth) removed. The remaining 2,589 points, distributed across 20 east-west transects, reported depths of 0.5–198 m (Figure 3).

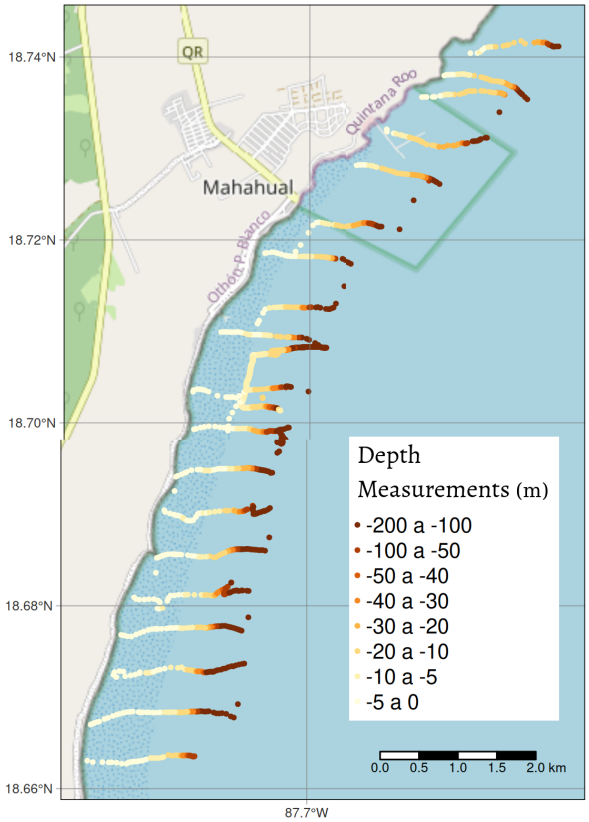

Figure 3. Distribution of *in situ* bathymetry points.

Landsat 9 (15/01/2023), SuperDove (17/01/2023), and Sentinel-2 (20/07/2022) images were selected, masked, and processed with n=10,000 and blue-green band ratios (Bands 2 and 4 for

Landsat/Sentinel; Bands 2 and 4 for SuperDove). Outliers (outside 1st–99th percentiles) were excluded. Figure 4 shows ratio values along a transect, with darker tones indicating greater depth. Spatial resolution differences among sensors are evident (see Table 1).

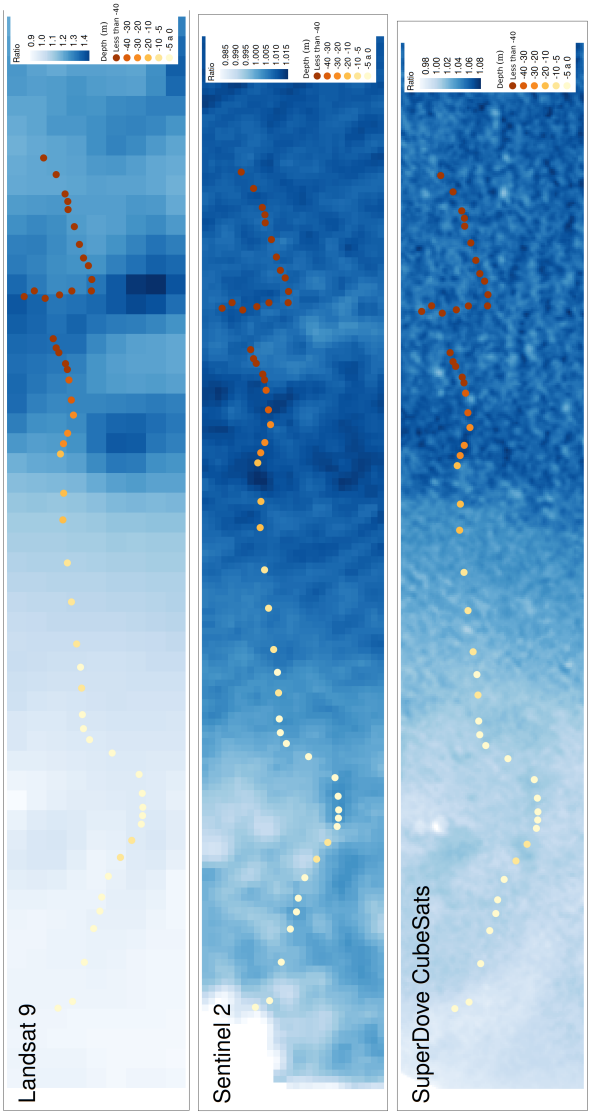

Figure 4. Sample ratio images derived from Landsat, Sentinel, and SuperDove data. According to Stumpf et al. (2003), these ratio values exhibit a linear relationship with depth up to 25 m in clear waters.

Figure 5 displays adjusted R^2 values for linear regression models (with/without glint correction and filtering) across depth ranges (10–35 m). Landsat 9 performed best without glint correction but with filtering (peak R^2 at 10–24 m). Sentinel-2 and SuperDove achieved optimal fits with both corrections, though Sentinel-2's R^2 declined rapidly with depth. Final models used depths of 0.5–24 m (Landsat/SuperDove) and 0.5–21 m (Sentinel).

Figure 6 illustrates nonlinearity beyond specific depths, with shallow points (depth < 5 m) also deviating from the model, explaining R^2 trends in Figure 5. Regularized regression and random forest models allow obtaining a better fit (see Fig. 7 for Landsat).

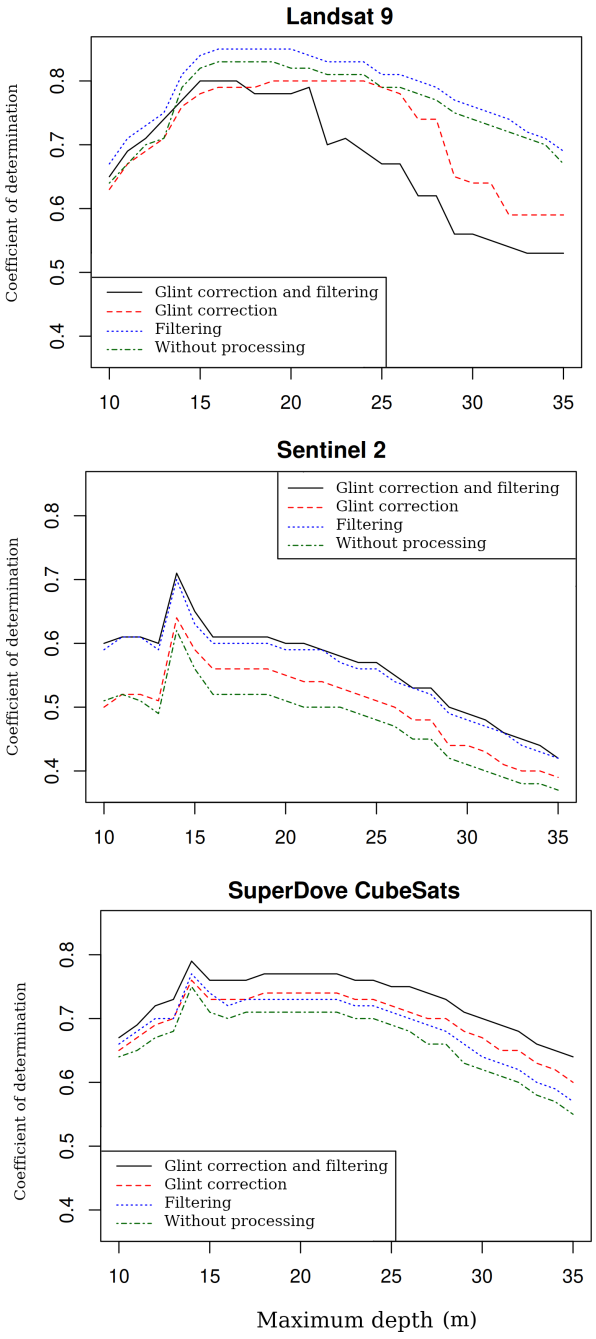

Figure 5. Variation of correlation coefficients between ratio values and depth obtained using: (a) different maximum depth thresholds, and (b) different preprocessing approaches (glint correction and filtering).

Table 2 shows the RMSE and MAE values obtained for each type of image and each modeling method. For the linear regression approach, RMSE values were 2.03 m (Landsat), 3.02 m (Sentinel), and 2.55 m (SuperDove). The regularized regression, and even more so, the random forest models allow for a significant reduction in the quantity of error, resulting in an RMSE error lower than one meter in the case of Landsat and Sentinel images. Figure 8 shows residuals concentrated near -5 m and -20 m, consistent with Figure 6. Figure 9 confirms residual correlation with depth and across models.

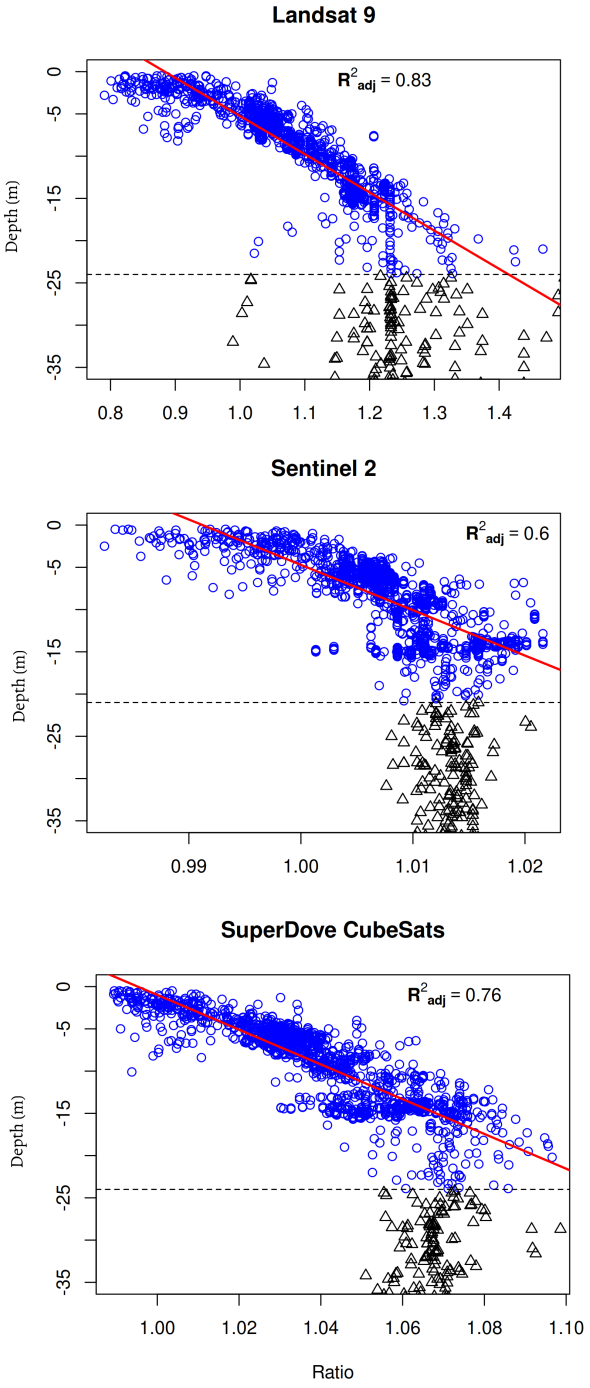

Figure 6. Scatter plot of ratio values *versus* depth. Blue circles represent data points included in the linear regression model, while triangles indicate depths beyond the reliable estimation range. The red line shows the regression fit, and the horizontal line marks the depth threshold separating modeled and excluded data.

6. Discussion

This study evaluated Stumpf et al.'s (2003) empirical ratio transform algorithm for bathymetric mapping in the Mexican Caribbean using Landsat 9, Sentinel-2, and SuperDove imagery, as well as different modeling approaches, including linear regression, regularized regression, and random forest. Results confirm its effectiveness for depths up to 20–24 m, with limitations in deeper and very shallow zones. Preprocessing (glint correction, filtering) significantly improved accuracy.

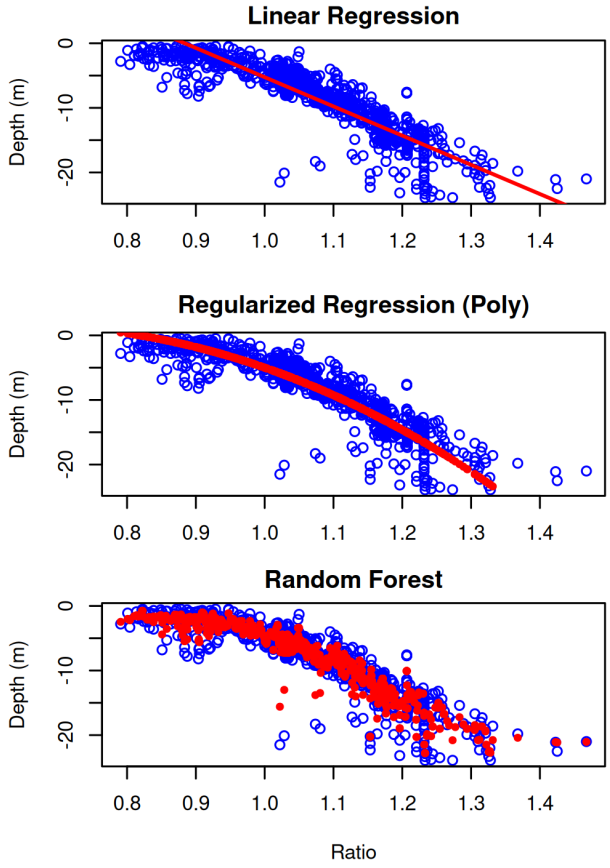

Figure 7. Scatter plot of ratio values *versus* depth (Landsat data). Blue circles represent data points, while the fitted models (linear regression, regularized polynomial regression, and random forest) are represented in red.

Glint correction was unnecessary for Landsat, likely due to its lower spatial resolution (30 m vs. Sentinel-2's 10 m and SuperDove's 3 m), which inherently smooths wave effects. Filtering (3x3 window) enhanced results by removing spectral outliers, but reduced spatial resolution, which can be problematic in areas with abrupt depth changes (e.g., reefs).

The models used in the present study allow for predicting depth with similar errors to those reported in other studies carried out in different parts of the world (Table 3).

Sensor	Fitting method	RMSE	MAE
Landsat	Linear Regression	2.03	1.48
	Regularized Regression	1.87	1.28
	Random Forest	0.88	0.56
Sentinel	Linear Regression	3.02	2.42
	Regularized Regression	3.01	2.41
	Random Forest	0.79	0.45
SuperDove	Linear Regression	2.55	1.90
	Regularized Regression	2.54	1.88
	Random Forest	1.02	0.60

Table 2. RMSE and MAE values of the models using different types of images and models.

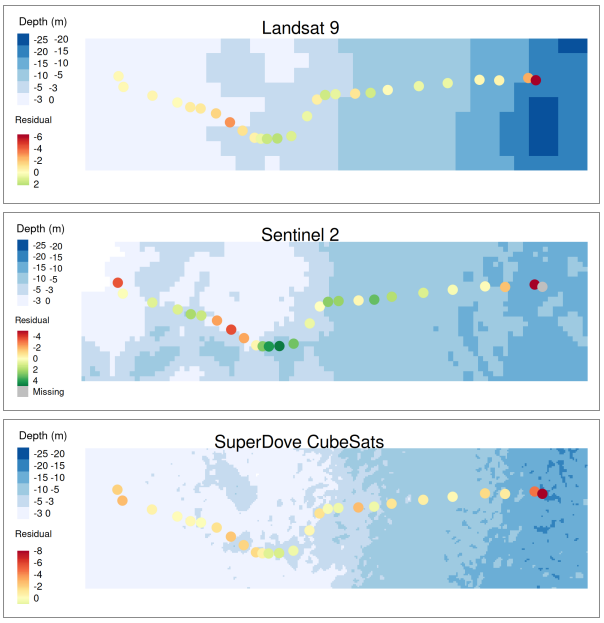

Figure 8. Sample bathymetric maps derived from Landsat, Sentinel, and SuperDove imagery (linear regression). Circle colors represent residual values (difference between predicted and observed depths) in the case of the linear regression.

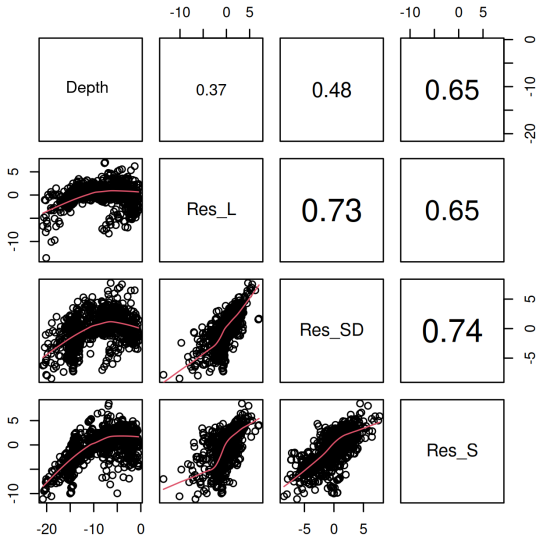

Figure 9. Correlation between: (a) residuals from all three bathymetric models, and (b) residuals *versus* depth measurements.

The study highlights the importance of assessing attenuation effects on maximum penetrable depth to define model limits. Vanderstraete et al. (2003) similarly recommend pre-mapping penetration depth before bathymetric estimation.

Performance was moderate across all sensors, with Landsat 9 achieving the lowest RMSE (2.03 m) using the linear regression and Sentinel (RMSE = 0.79m) with random forest. More flexible models based on machine learning enable us to obtain a better fit because the relationship between the depth and the

Authors	Study area	Sensor	RMSE (m)
Jawak y Luis	Larsemann, Antartica	Worldview-2	0.23-1.2
Vanderstraete et al. (2003)	Red sea, Egypt	Landsat 7	2.4
Pratomo et al. (2024)	Gili-Noko, Java	Sentinel-2	1.7
Casal et al. (2020)	Irland coast	Sentinel-2	0.6 – 1.5
	Gaunquan and Oahu islands,	Landsat 8	0.4-4.3
Duan et al. (2022)	Sea of China	Sentinel-2	0.4-4.1
Hernandez y Armstrong (2016)	Carribean, Puerto Rico	Worldview-2	1.6
		PlanetScope	0.4
Gabr et al. (2020)	Mediterranean sea, Egypt	Landsat 8	0.4-0.5
		Landsat 8	1.9-10.2
Gülher y Alganci (2023)	Horseshoe island, Antartica	Sentinel-2	3.6-5.9
	Bahias Mobile and Tamapa,	Landsat 8	2.3-2.8
Yunus et al., 2019	Golf of Mexico	Sentinel-2	2.5
Perea-Ardila y Oviedo-Barrero (2020)	Bahía Solano, Pacific, Colombia	Landsat 8	1.5

Table 3. RMSE errors reported in different studies using empirical methods and multispectral images.

ratio is not a perfect linear relation. Discrepancies in the results between images may stem from differing acquisition dates and conditions (waves, water clarity). For instance, Hedley et al. (2018) found no greater dispersion in Sentinel-2 *versus* Landsat 8, contrary to our results.

Residuals were highest in very shallow waters (0–5 m), possibly due to seabed variability or high bottom reflectance (Gao, 2009). These errors minimally impacted deeper estimates.

Future studies could explore alternative atmospheric corrections, hybrid empirical-analytical algorithms, and applications in monitoring systems (Ariza and Ramírez, 2014; Pacheco et al., 2015) or inland waters (Jawak and Luis, 2015; Yang et al., 2022).

7. Conclusions

This study demonstrates the utility of multispectral satellite data and Stumpf et al.'s (2003) ratio transform method for estimating bathymetry in shallow coastal waters. The methodology provides reasonably accurate depth estimates (up to 20 m) in clear water, with precision heavily dependent on image preprocessing (masking, glint correction, and filtering) and the ap-

proach used to fit the model. The random forest method enables more precise results.

Further research should investigate alternative atmospheric corrections, hybrid algorithms, and applications in seabed change detection and inland water bodies.

Acknowledgements

This study was carried out within the scope of the PAPIIT-UNAM project (IN112823) entitled: *Azolvamiento y eutroficación en presas periurbanas de zonas templadas de México: contribuciones para su evaluación y prospección*.

References

Abdul Gafoor, F., Al-Shehhi, M. R., Cho, C.-S., Ghedira, H., 2022. Gradient Boosting and Linear Regression for Estimating Coastal Bathymetry Based on Sentinel-2 Images. *Remote Sensing*, 14(9), 5037. https://doi.org/10.3390/rs14195037.

Ariza, A., Ramírez, H., 2014. Modelo Batimétrico derivado de imágenes Landsat ETM+ en zonas de arrecifes tropicales. *Revista Cartográfica*, 90, 43-58.

Ashphaq, M., Srivastava, P. K., Mitra, D., 2021. Review of near-shore satellite derived bathymetry: Classification and account of five decades of coastal bathymetry research. *Journal of Ocean Engineering and Science*, 6(4), 340-359. https://doi.org/10.1016/j.joes.2021.02.006.

Casal, G., Harris, P., Monteys, X., Hedley, J., Cahalane, C., McCarthy, T., 2020. Understanding satellite-derived bathymetry using Sentinel 2 imagery and spatial prediction models. *GIScience & Remote Sensing*, 57(3), 271–286. https://doi.org/10.1080/15481603.2019.1685198.

Casal, G., Monteys, X., Hedley, J., Harris, P., Cahalane, C., McCarthy, T., 2019. Assessment of empirical algorithms for bathymetry extraction using Sentinel-2 data. *International Journal of Remote Sensing*, 40(8), 2855–2879. https://doi.org/10.1080/01431161.2018.1533660.

Duan, Z., Chu, S., Cheng, L., Ji, C., Li, M., Shen, W., 2022. Satellite-derived bathymetry using Landsat-8 and Sentinel-2A images: assessment of atmospheric correction algorithms and depth derivation models in shallow waters. *Opt. Express*, 30(3), 3238–3261. https://doi.org/10.1364/OE.444557.

Equipo Planeta, 2017. Interfaz del programa de aplicación Planet: en el espacio para la vida en la tierra. San Francisco, CA.

Gabr, B., Ahmed, M., Marmoush, Y., 2020. Planet-Scope and Landsat 8 Imageries for Bathymetry Mapping. *Journal of Marine Science and Engineering*, 8(2), 143. https://doi.org/10.3390/jmse8020143.

Gao, J., 2009. Bathymetric mapping by means of remote sensing. *Progress in Physical Geography*, 33(1), 103-116. https://doi.org/10.1177/0309133309105657.

Gülher, E., Alganci, U., 2023. Satellite-Derived Bathymetry Mapping on Horseshoe Island, Antarctic Peninsula, with Open-Source Satellite Images: Evaluation of Atmospheric Correction Methods and Empirical Models. 15(10), 2568. https://doi.org/10.3390/rs15102568.

Hedley, J. D., Harborne, A. R., Mumby, P. J., 2005. Technical note: Simple and robust removal of sun glint for mapping shallow-water benthos. *International Journal of Remote Sensing*, 26(10), 2107–2112. https://doi.org/10.1080/01431160500034086.

Hedley, J. D., Roelfsema, C., Brando, V., Giardino, C., Kutser, T., Phinn, S., Mumby, P. J., Barrilero, O., Laporte, J., Koetz, B., 2018. Coral reef applications of Sentinel-2: Coverage, characteristics, bathymetry and benthic mapping with comparison to Landsat 8. *Remote Sensing of Environment*, 216, 598-614. https://doi.org/10.1016/j.rse.2018.07.014.

Hernandez, W. J., Armstrong, R. A., 2016. Deriving Bathymetry from Multispectral Remote Sensing Data. *Journal of Marine Science and Engineering*, 4(1), 8. https://doi.org/10.3390/jmse4010008.

Jagalingam, P., Akshaya, B., Hegde, A. V., 2015. Bathymetry Mapping Using Landsat 8 Satellite Imagery. *Procedia Engineering*, 116, 560-566. https://doi.org/10.1016/j.proeng.2015.08.326. 8th International Conference on Asian and Pacific Coasts (APAC 2015).

Jawak, S., Luis, A., 2015. Spectral Information Analysis for the Semiautomatic Derivation of Shallow Lake Bathymetry Using High-resolution Multispectral Imagery: A Case Study of Antarctic Coastal Oasis. *Aquatic Procedia*, 4, 1331-1338. https://doi.org/10.1016/j.aqpro.2015.02.173.

Lyzenga, D., 1978. Passive remote sensing techniques for mapping water depth. *Applied Optics*, 17(3), 379-383.

Lyzenga, D., 1981. Remote sensing of bottom reflecatnce and water attenuation parameters in shallow water using aircarft and Landsat data. *International Journal of Remote Sensing*, 2(1), 71-82. https://doi.org/10.1080/01431168108948342.

Lyzenga, D., Malinas, N., Tanis, F., 2006. Multispectral bathymetry using a simple physically based algorithm. *IEEE Transactions on Geoscience and Remote Sensing*, 44(8), 2251-2259. https://doi.org/10.1109/TGRS.2006.872909.

Merediz-Alonso, G., 2012. Puntos batimétricos de la reserva de la biosfera de sian ka'an y arrecifes de sian ka'an'. Technical report, CONABIO, Amigos de Sian Ka'an. Proyecto: DM011, Caracterización y monitoreo de la condición arrecifal en cinco Áreas Naturales Protegidas y un área de influencia de Quintana Roo, México.

Pacheco, A., Horta, J., Loureiro, C., Ferreira, O., 2015. Retrieval of Nearshore Bathymetry from Landsat 8 Images: A Tool for Coastal Monitoring. *Remote Sensing of Environment*, 159, 102-116. https://doi.org/10.1016/j.rse.2014.12.004.

Perea-Ardila, M. A., Oviedo-Barrero, F., 2020. Satellite-derived bathymetry (SDB): an approach to bathymetric cartography with multispectral images in shallow waters of Bahía Solano, Colombia. *Revista Ciencias Marinas Y Costeras*, 12(1), 117-134. https://doi.org/10.15359/revmar.12-1.6.

Philpot, W. D., 1989. Bathymetric mapping with passive multispectral imagery. *Appl. Opt.*, 28(8), 1569–1578. https://doi.org/10.1364/AO.28.001569.

Pratomo, Danar Guruh, Cahyadi, Mokhamad Nur, Hariyanto, Irena Hana, Syariz, Muhammad Aldila, Putri, Shofa' Amaliah, 2024. Lyzenga Algorithm for Shallow

Water Mapping Using Multispectral Sentinel-2 Imageries in Gili Noko Waters. *BIO Web Conf.*, 89, 07006. https://doi.org/10.1051/bioconf/20248907006.

R Core Team, 2025. R: A Language and Environment for Statistical Computing. R Foundation for Statistical Computing, Vienna, Austria.

Stumpf, R., Holderied, K., Sinclair, M., 2003. Determination of water depth with high-resolution satellite imagery over variable bottom types. *Limnology and Oceanography*, 48(1), 547-556. https://doi.org/10.4319/lo.2003.48.1_part_2.0547.

Su, H., Liu, H., Heyman, W., 2008. Automated Derivation of Bathymetric Information from Multi-Spectral Satellite Imagery Using a Non-Linear Inversion Model. *Marine Geodesy*, 31(4), 281-298.

Sánchez-Carnero, N., Ojeda-Zujar, J., Rodríguez-Pérez, D., Marquez-Perez, J., 2014. Assessment of different models for bathymetry calculation using SPOT multispectral images in a high-turbidity area: the mouth of the Guadiana Estuary. *International Journal of Remote Sensing*, 35(2), 493–514. https://doi.org/10.1080/01431161.2013.871402.

Valderrama-Landeros, L., R., M.-D., Ressl, R., R., S. C., Cruz-Ramírez, C., Muñoz-Pérez, J., 2019. Coastal erosion in Quintana Roo. *Journal of Geographical Sciences*, 29, 1637-1654. https://doi.org/10.1007/s11442-019-1679-x.

Vanderstraete, T., Goossens, R., T.K., G., 2003. Remote sensing as a tool for bathymetric mapping of coral reefs in the Red Sea (Hurghada – Egypt). *Belgeo*, 3, 257-268. https://doi.org/10.4000/belgeo.16652.

Yang, H., Ju, J., Guo, H., Qiao, B., Nie, B., Zhu, L., 2022. Bathymetric Inversion and Mapping of Two Shallow Lakes Using Sentinel-2 Imagery and Bathymetry Data in the Central Tibetan Plateau. *IEEE Journal of Selected Topics in Applied Earth Observations and Remote Sensing*, 15, 4279-4296. https://doi.org/10.1109/JSTARS.2022.3177227.

Yunus, A. P., Dou, J., Song, X., Avtar, R., 2019. Improved Bathymetric Mapping of Coastal and Lake Environments Using Sentinel-2 and Landsat-8 Images. *Sensors*, 19(12), 2788. https://doi.org/10.3390/s19122788.